







## RESEARCH ARTICLE

## SAR and temperature distributions in a database of realistic human models for 7 T cardiac imaging

Bart R. Steensma<sup>1</sup>  | Ettore F. Melià<sup>1,2</sup>  | Peter Luijten<sup>1</sup>  |  
Dennis W. J. Klomp<sup>1</sup>  | Cornelis A. T. van den Berg<sup>1</sup>  | Alexander J. E. Raaijmakers<sup>3</sup> <sup>1</sup>Center for Image Sciences, University Medical Center Utrecht, Utrecht, The Netherlands<sup>2</sup>Tesla Dynamic Coils, Zaltbommel, The Netherlands<sup>3</sup>Biomedical Engineering, Eindhoven University of Technology, Eindhoven, The Netherlands**Correspondence**Bart R. Steensma, Heidelberglaan 100, 3584 CX, Utrecht, The Netherlands.  
Email: b.r.steensma@umcutrecht.nl**Funding information**

Dutch Research Council (NWO), Grant/Award Number: grant number: 15739

**Purpose:** To investigate inter-subject variability of  $B_1^+$ , SAR and temperature rise in a database of human models using a local transmit array for 7 T cardiac imaging.**Methods:** Dixon images were acquired of 14 subjects and segmented in dielectric models with an eight-channel local transmit array positioned around the torso for cardiac imaging. EM simulations were done to calculate SAR distributions. Based on the SAR distributions, temperature simulations were performed for exposure times of 6 min and 30 min. Peak local SAR and temperature rise levels were calculated for different RF shim settings. A statistical analysis of the resulting peak local SAR and temperature rise levels was performed to arrive at safe power limits.**Results:** For RF shim vectors with random phase and uniformly distributed power, a safe average power limit of 35.7 W was determined (first level controlled mode). When RF amplitude and phase shimming was performed on the heart, a safe average power limit of 35.0 W was found. According to Pennes' model, our numerical study suggests a very low probability of exceeding the absolute local temperature limit of 40 °C for a total exposure time of 6 min and a peak local SAR of 20 W/kg. For a 30 min exposure time at 20 W/kg, it was shown that the absolute temperature limit can be exceeded in the case where perfusion does not change with temperature.**Conclusion:** Safe power constraints were found for 7 T cardiac imaging with an eight-channel local transmit array, while considering the inter-subject variability of  $B_1^+$ , SAR and temperature rise.**KEYWORDS**

7 T, cardiac imaging, fractionated dipole, safety, specific absorption rate, temperature

## 1 | INTRODUCTION

The improved signal-to-noise ratio at 7 T allows for cardiac magnetic resonance (CMR) imaging at increased spatial resolution as compared with 1.5 T or 3 T.<sup>1–3</sup> Many sequences that are common for CMR at 1.5 T or 3 T, such as inversion recovery sequences, require a high flip angle and/or a short repetition time,<sup>4</sup> which leads to high RF power deposition. Because of increased local SAR levels at 7 T compared with 1.5 T or 3 T,<sup>5,6</sup> and

**Abbreviations:** CMR, cardiac magnetic resonance; FDTD, finite difference time domain; VOP, virtual observation point.

This is an open access article under the terms of the Creative Commons Attribution-NonCommercial-NoDerivs License, which permits use and distribution in any medium, provided the original work is properly cited, the use is non-commercial and no modifications or adaptations are made.

© 2021 The Authors. *NMR in Biomedicine* published by John Wiley & Sons Ltd.

because local transmit arrays are used instead of a volume body coil (thereby enforcing local SAR limitations), limits on allowable average power are more stringent at 7 T. These more stringent power constraints mean that standard CMR sequences are not easily applicable at 7 T.

7 T cardiac imaging is typically done using a local transmit array. These arrays typically consist of multiple transmit channels for which the phase and amplitude can be controlled. Normally in 7 T cardiac imaging, subject-specific calibration of the phases and amplitudes (RF shimming) is used to achieve an efficient and uniform transmit field in the heart. To ensure that the patient is not exposed to severe local tissue heating, local SAR is used as a metric to constrain the RF input of a local transmit array. The peak local SAR level cannot exceed predefined limits, which are described by the IEC.<sup>7</sup> As also described by the IEC, local SAR is averaged over a volume containing a total mass of 10 g. Since local SAR cannot practically be measured in vivo, average power limits are typically derived from electromagnetic simulations—using, eg, the finite difference time domain (FDTD) method—on generic human models.<sup>8</sup> These generic human models normally do not match well to the geometry of the subject in the scanner; therefore, an additional safety factor needs to be used, which accounts for inter-subject variability.<sup>9–13</sup> The use of this safety factor ensures that peak local SAR limits are never exceeded when the patient anatomy does not match the anatomy of the simulation model, but can lead to severe overestimation of the actual peak local SAR, resulting in overly conservative power constraints and increased examination times.

Inter-subject variability has a strong influence on peak SAR levels for various imaging targets at 7 T. Previous studies have investigated inter-subject variability for multi-transmit head imaging.<sup>10,12</sup> De Greef et al<sup>12</sup> investigated SAR levels for six different head models of the Virtual Family and Virtual Classroom; these models originated from manual segmentation.<sup>8</sup> Le Garrec et al<sup>10</sup> used an in-house generated, surface based head model to generate a database of 33 transformed head models. From this database, it was possible to sample the parameter space of head length, breadth and shift in the Z- and Y-directions following an unscented transform scheme. Peak SAR values were calculated for several RF excitation schemes. For body imaging at 7 T, the inter-subject variability of SAR has been studied for two dipole arrays in a prostate imaging setup.<sup>11,13</sup> Ipek et al studied inter-subject variability of peak local SAR for a single-side adapted dipole array on four different dielectric models,<sup>13,14</sup> which were generated from manual segmentation of Dixon scans with the 7 T transmit array in place. More recently, Meliàdò et al. presented a more rigorous approach where an automated pipeline was created to generate a simulation model from a Dixon scan with a mock-up array and landmarks in place. Using this method, 23 custom-built dielectric models were simulated for the fractionated dipole array to derive power limits for RF shimming on the prostate or for multidimensional pulses.<sup>11</sup>

Similar studies for 7 T cardiac imaging are currently still missing. Therefore, the first aim of this work is to investigate inter-subject variability for cardiac imaging at 7 T in a database of custom-built dielectric models, using an approach similar to the one used by Meliàdò et al.<sup>11</sup> A probabilistic analysis of 10 g averaged peak local SAR levels for different RF shim phases and subjects was applied to arrive at local SAR levels that have a probability of less than 0.1% of being exceeded (pSAR<sub>99</sub>). These local SAR levels were then used to derive average power limits on a per channel basis. The methods that we used for SAR analysis are the same as used in Meliàdò et al<sup>11</sup>; however, we have added a more elaborate evaluation of SAR for different RF shimming methods.

The second aim of this work was to extend the SAR analysis by also incorporating temperature simulations, which were not included in the work of Meliàdò et al.<sup>11</sup> Similar studies have been done before for brain imaging,<sup>15–17</sup> for imaging near a hip implant<sup>18</sup> and for breast imaging,<sup>19</sup> but not including a statistical analysis for 7 T cardiac imaging. The temperature simulations were done for heating intervals of 6 and 30 min. For the 6 min scenario, it was ensured that our method to simulate temperature was accurate for exposure levels at the SAR limit, whereas the second scenario corresponded to a realistic examination time for a 7 T cardiac examination. By including temperature simulations in our analysis, it became possible to study inter-subject variation for temperature and to study the relation between local SAR and temperature rise under various circumstances.

## 2 | METHODS

### 2.1 | Model generation

After obtaining IRB approval and written informed consent from each subject, 14 subjects (age 25–54, BMI 18–26) were scanned at 1.5 T (Philips Ingenia, Philips Healthcare, Best, The Netherlands) with a mockup array in place to achieve realistic body deformation. A 3D RF spoiled GRE multi-echo Dixon scan ( $T_R/T_{E1}/T_{E2} = 5.56/1.64/3.76$  ms, resolution  $1.7 \times 1.7 \times 2.5$  mm<sup>3</sup>, FOV  $50 \times 50 \times 40$  cm<sup>3</sup>, acquisition time 57 s, free breathing) was acquired to calculate water, fat, in-phase and out-of-phase images which were segmented<sup>20</sup> into three tissue types (bone, fat and muscle). Because of breathing and cardiac motion images were blurred, but this did not affect the segmentation. The segmented images were imported into iSeg (ZMT, Zürich, Switzerland), where a 4 mm layer of skin was added around the body models. The body models were cropped beyond the field of view of the MRI acquisition. The four tissues were assigned with the following electrical and thermal properties.<sup>21,22</sup>

The validity of a three-tissue model (lung, muscle and fatty tissue) versus a full dielectric model has been demonstrated before for local SAR.<sup>13,23,24</sup> For temperature, it was found necessary to also include skin (leading to a four-tissue model) in the model. Skin has a high perfusion rate and significantly affects local temperature.<sup>25</sup> As an additional validation step, SAR and thermal simulations were done with the fully segmented body model Duke and compared with a four-tissue model of Duke. It was shown that the four-tissue model slightly overestimates peak

SAR in one scenario (17 W/kg for the four-tissue model compared with 16 W/kg for the full model; Figures S1 and S2). Local temperature rise in the heart was also slightly overestimated for the four-tissue model because the full model has higher perfusion values in blood and heart muscle. It was also observed that for the four-tissue body model the temperature in the spinal cord can be overestimated, because in the full body model the spinal cord tissue has a very high perfusion value. This was not the case in the four-tissue model.

## 2.2 | EM simulations

### 2.2.1 | Simulation settings

FDTD simulations were done in Sim4Life V3.4 (Zurich MedTech, Zurich, Switzerland) to calculate EM-field distributions in the segmented body model. An eight-channel dipole array was modelled as the transmit coil.<sup>3,26</sup> The eight dipole antennas were matched with two series capacitors of 18 pF. All simulation models were voxelized with an adaptive grid using a maximum resolution of  $0.7 \times 0.7 \times 0.7 \text{ mm}^3$ , resulting in approximately 30 million voxels per simulation model. EM simulations were done on a GPU (Tesla K20, Nvidia, Santa Clara, CA); simulations took approximately 30 min per simulated port in the model (eight ports per model). Similar to the work of Boulant et al,<sup>16</sup> all simulation results were regridded to a  $4 \times 4 \times 4 \text{ mm}^3$  rectangular grid to make the SAR and temperature calculations less computationally demanding. SAR and temperature calculations were done on a PC (32 GB RAM, Intel Xeon E3-1220 CPU @ 3.10 GHz; Intel, Santa Clara, CA). 10 g averaged  $Q$ -matrices<sup>27,28</sup> and virtual observation points (VOPs)<sup>29</sup> were calculated for every model to enable rapid calculation of peak SAR levels for arbitrary RF shims. To enable fast calculation of and to minimize the number of VOPs, the generalized VOP method as described by Lee et al<sup>30</sup> was implemented, in combination with the acceleration method demonstrated by Kuehne et al.<sup>31</sup> VOPs were calculated with an overestimation of 5%. Specifically for the temperature simulations, the electric fields for every transmit channel were filtered with a  $3 \times 3 \times 3$  median filter, to remove spikes due to staircasing errors in the FDTD simulations.<sup>16</sup> This was not done for the SAR calculations as they were already smoothed by the 10 g averaging procedure.

### 2.2.2 | SAR analysis

A statistical analysis on the distribution of peak SAR levels was performed by calculating peak SAR values for every subject for 100 000 random RF shims (14 models in total; the same RF shims were used for all models). Peak SAR was calculated for randomly distributed transmit phases (range between 0 and  $2\pi$ , according to a uniform distribution and equally distributed total input power of 1 W (0.125 W per channel). By doing so, all possible peak SAR levels in MR experiments with phase-only RF shimming were sampled. To also include a scenario where power was distributed non-uniformly over the channels, we calculated the maximum eigenvalue of the  $Q$ -matrices. Additionally, the upper limit worst-case SAR for phase-only shimming was calculated according to the fast upper bound method of Meliadó et al.<sup>32</sup> Results of the SAR calculations were plotted in a histogram of peak SAR values for all volunteers and all random RF shims, similar to the histograms shown in the work of Meliadó et al.<sup>11</sup> The resulting distribution corresponds to a gamma distribution, for which a shape-parameter  $k$  and a scale parameter  $\theta$  were fitted. By fitting a distribution to the histogram data, it was possible to make statistical predictions on the SAR levels over the entire population, under the assumption that our model database was a representative sample of the population. In this case, we defined a peak local SAR level that had a probability of less than 0.1% of being exceeded for any subject and any RF shims. This SAR level is referred to throughout this manuscript as the  $p\text{SAR}_{99}$  level.

## 2.3 | Temperature simulations

### 2.3.1 | Temperature simulation settings

Temperature rise in the human body as a result of exposure to a SAR distribution was modelled using Pennes' bioheat equation<sup>33</sup>:

$$\rho c_p \frac{\delta T}{\delta t} = \nabla \cdot (k \nabla T) + W_b c_b (T_b - T) + C + \rho \text{SAR} \quad (1)$$

where  $\rho$  is mass density ( $\text{kg}/\text{m}^3$ ),  $c_p$  is the specific heat capacity ( $\text{J}/\text{kg}/\text{K}$ ),  $k$  is the thermal conductivity ( $\text{W}/\text{K}/\text{m}$ ),  $W_b$  is the blood perfusion constant ( $\text{kg}/\text{m}^3/\text{s}$ ),  $c_b$  is the blood specific heat capacity ( $\text{J}/\text{kg}/\text{K}$ ),  $T_b$  is the temperature of blood (set to  $37^\circ\text{C}$ ),  $C$  is the metabolic heat generation ( $\text{W}/\text{m}^3$ ) and finally  $\rho \text{SAR}$  is the heat generation from external sources. Pennes bioheat equation can be separated into an equilibrium temperature component ( $T_{00}$ ), which was assumed to remain constant, and a temperature rise component ( $T_{\text{rise}}$ ).<sup>16,17,34</sup> If the equilibrium temperature  $T_{00}$  is

known, which can be obtained by solving Equation 1 without the SAR term present, the final temperature can be calculated as  $T = T_{00} + T_{rise}$ . For the equilibrium temperature, it was assumed that metabolic heat generation remains constant and is in equilibrium with cooling by blood. The equilibrium temperature and the temperature rise components were modelled as the following:

$$\rho c_p \frac{\delta T_{rise}}{\delta t} = \nabla \cdot (k \nabla T_{rise}) - W_b c_b T_{rise} + \rho SAR \quad (2a)$$

$$\rho c_p \frac{\delta T_{00}}{\delta t} = \nabla \cdot (k \nabla T_{00}) + W_b c_b (T_b - T_{00}) + C = 0. \quad (2b)$$

For a multi-channel transmit array, the SAR distribution of all combined channels given an RF shim vector  $\mathbf{v}$  was expressed using the Q-matrix formalism:

$$SAR = \mathbf{v}^H \mathbf{Q} \mathbf{v}. \quad (3)$$

In Equation 3, a local Q-matrix ( $N_c \times N_c$ ) exists for every voxel;  $N_c$  indicates the number of transmit channels and every entry of the Q-matrix corresponds to a certain combination of transmit channels. Since the solution of Equation 2 scales linearly with SAR, the temperature rise can be expressed with a similar formalism<sup>16,34</sup>:

$$T_{rise} = \mathbf{v}^H \mathbf{T}_{rise} \mathbf{v}. \quad (4)$$

$$\mathbf{T}_{rise} = \begin{pmatrix} T_{1,1} & \cdots & T_{1,N} \\ \vdots & \ddots & \vdots \\ T_{N,1} & \cdots & T_{N,N} \end{pmatrix}. \quad (5)$$

The entries of  $\mathbf{T}_{rise}$  correspond to a single solution of the Pennes' bioheat equation that exist for every combination of transmit channels  $i, j$ :

$$\rho c_p \frac{\delta T_{rise,ij}}{\delta t} = \nabla \cdot k \nabla T_{rise,ij} + W_b c_b (-T_{rise,ij}) + \rho SAR_{ij}. \quad (6)$$

Equation 6 was solved for every combination of transmit channels ( $i, j$ ) and a pre-defined heating interval to fill the entries of the  $\mathbf{T}_{rise}$  matrix. Equation 4 was then used to calculate temperature rise quickly for every RF shim vector  $\mathbf{v}$ . A MATLAB (MathWorks, Natick, MA) based temperature solver available online<sup>35,36</sup> was used to solve Pennes' bioheat equation for every entry of the Q-matrix to obtain a temperature matrix  $\mathbf{T}_{rise}$  for every model. Pennes' bioheat equation was solved for a total heating time of 6 min and for a heating time of 30 min, during which we expect that steady-state temperature is approximated. To check the validity of the latter statement, we simulated temperature versus time for a single human model. This was done for two scenarios: one with constant perfusion parameters and one with perfusion parameters that increase with temperature,<sup>37</sup> using the same model as Murbach et al.<sup>38</sup> Only the approach with constant perfusion parameters was compatible with the temperature VOP model, since the temperature rise should scale linearly with input power. Based on the temperature matrix, temperature VOPs were derived for rapid calculation of temperature rise for different RF shim drives.<sup>16,34</sup> To derive the temperature VOPs, the same algorithm was used as for derivation of VOPs from the SAR Q-matrices.

### 2.3.2 | Peak $\Delta T$ analysis

Since the resulting temperature rise matrix  $\mathbf{T}_{rise}$  depended strongly on the defined heating interval, temperature simulations were done separately for the two heating intervals (6 min and 30 min) using the perfusion values from Table 1. Based on the simulated  $\mathbf{T}_{rise}$  matrices, temperature VOPs<sup>16,34</sup> were calculated for the two different heating scenarios. Based on the temperature VOPs, peak  $\Delta T$  values were calculated for the same 100 000 random RF shims as were used in the SAR analysis for all 14 volunteers. The resulting  $\Delta T$  values were plotted as histograms for all volunteers and RF shims together, which were used to fit gamma-distributions in order to carry out a probabilistic analysis of peak  $\Delta T$  values. For all models, a peak  $\Delta T$  value was found that has a chance of less than 0.1% of being exceeded for a random RF shim ( $p\Delta T_{99}$ ). The final result of this procedure was three  $\Delta T$  histograms and two fitted  $p\Delta T_{99}$  values ( $p\Delta T_{99,6 \text{ min}}$  and  $p\Delta T_{99,30 \text{ min}}$  according to the two heating intervals).



**TABLE 1** Electric and thermal tissue parameters of muscle, fat, skin and lung tissue from the ITIS database<sup>21</sup>

Tissue type	Conductivity [S/m] @ 298 MHz	Relative permittivity [a.u.] @ 298 MHz	Specific heat capacity [J/kg/K]	Thermal conductivity [W/m/K]	Heat generation rate [W/kg]	Perfusion rate [kg/m <sup>3</sup> /s]	Mass density [kg/m <sup>3</sup> ]
Muscle	0.77	58.22	3421	0.495	0.9061	0.71	1090.4
Fat	0.08	11.75	2348	0.2115	0.5066	0.53	911
Skin	0.64	49.89	3391	0.3722	1.648	2.1	1109
Lung	0.36	24.80	3886	0.3874	6.209	7.44	394

## 2.4 | RF shimmed SAR and temperature analysis

Based on the simulated per-channel  $B_1^+$  distributions, subject-specific RF shim drives were calculated for all body models. A region of interest was drawn over the heart in a transverse 2D slice, after which three different RF shims were calculated for every model. For the “Max  $B_1^+$  shim” the average  $B_1^+$  in the heart was maximized using phase-only shimming with power distributed equally over all channels. This corresponds to the method we mostly use at our site. For the “uniformity shim” the coefficient of variation ( $\frac{\sigma}{\mu}$ ) in the heart ROI was minimized. Both amplitude and phase were included in the optimization. For the “tradeoff” shim, a target function  $f$  was calculated, which was a tradeoff between average  $B_1^+$  and coefficient of variation ( $f = \mu + 2\frac{\sigma}{\mu}$ ). Again, both amplitude and phase were optimized. The optimal RF shim vectors were calculated in MATLAB using the constrained minimization procedure `fmincon`. Total input power was kept equal to 1 W, with a maximum input power of 1 W per channel and a minimum input power of 0.06 W per channel. The optimization was initialized five times with random input phases and amplitudes to reduce the likelihood of converging to a local minimum. Finally, a “universal RF shim” was found by optimizing the tradeoff target function, but at the same time for all volunteers. The aim of this was to investigate the feasibility of using a single RF shim for all volunteers in terms of imaging performance and safety. This approach is somewhat similar to the universal pulse concept<sup>39</sup>; however, we optimized only RF phase and amplitude and not gradient trajectories. For all shim settings,  $B_1^+$ ,  $SAR_{10g}$  and  $\Delta T$  distributions were calculated and compared on all body models. The similarity between these RF shims was evaluated by comparing the input phase and power for all volunteers and coil channels.

To calculate SAR and temperature rise for RF shimmed drive vectors, 100 000 random RF shims were found using three methods. For the first method, one of the optimal drive vectors (max  $B_1^+$ , homogeneity or tradeoff) was chosen. A random offset within a range of  $\pm 10\%$  was given on the phase and amplitude of every channel; this was repeated for all 100 000 RF shims. This procedure was done separately for all models, thus resulting in a distribution of SAR values for RF shims that were optimized individually, as is normally done on a multi-transmit system. For the second method, this procedure was repeated while using the same amplitude on all channels. For the third method, the same RF shims were used for all models. The universal RF shim was used as a starting point, for every ‘new’ RF shim within the set of 100 000, an offset within a range of  $\pm 10\%$  (uniform sampling) was given to all phases and amplitudes. This did not result in an optimal RF shim for the individual models, but could correspond to a scenario where a multi-transmit setup is not available.

## 2.5 | Correlation between peak $SAR_{10g}$ and $\Delta T$ and effect of model database size

As a result of the SAR and temperature analysis in Sections 2.2 and 2.3, peak  $SAR_{10g}$  and  $\Delta T$  values are calculated for a total of 100 000 RF shims (using the same RF shim each time to calculate peak  $SAR_{10g}$  and  $\Delta T$ ). As a final sanity check, the correlation (Pearson correlation coefficient, calculated using MATLAB) between peak  $SAR_{10g}$  and peak  $\Delta T$  was evaluated by combining all  $100\,000 \times 14$  p $SAR_{10g}$  and p $\Delta T$  values in a scatter plot. Finally, to investigate the effect of database size on our SAR and temperature predictions, we plotted SAR and temperature rise distributions when different numbers of models were left out of the database.

## 3 | RESULTS

### 3.1 | Model generation

Figure 1 shows the segmented body models including BMI, sex and age.

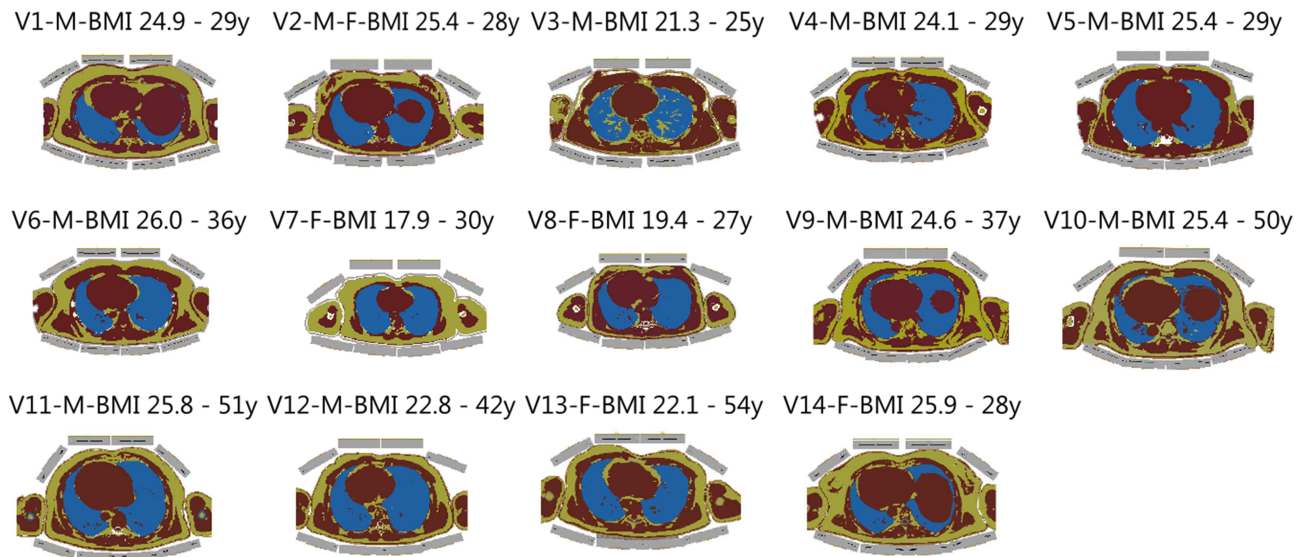


**FIGURE 1** Segmented models for every subject. Muscle indicated in red, fat in yellow, lung in blue and skin in light brown. Substrates of the antennas are indicated in grey

### 3.2 | EM simulations

Figure 2A shows peak SAR values over 100 000 random RF phase shims per model, also including the worst-case SAR values for random phases and the maximum eigenvalue of the Q-matrix. Figure 2B shows a histogram of these  $\text{SAR}_{10g}$  values for all 14 models. The resulting  $\text{pSAR}_{99}$  value from the fitted gamma distribution is 0.56 W/kg for a total input power of 1 W; the median  $\text{pSAR}$  value is 0.34 W/kg. The worst-case SAR predicted from the highest eigenvalue of the Q-matrix (red stars) is more than twice as high as the maximum SAR with phase-only variations (blue stars) in all volunteers. The worst-case SAR calculated with the method of Meliadori et al<sup>40</sup> corresponds to the highest SAR found over all RF shims.

### 3.3 | Temperature simulations

Figure 2C and 2D shows the peak temperature rise  $\text{p}\Delta T_{99,6\text{min}}$  for 1 W input power. The fitted gamma distribution (2D) results in a  $\text{p}\Delta T_{99,6\text{min}}$  of 0.061 °C and a median  $\Delta T$  of 0.035 °C. For a heating interval of 30 min we find that  $\text{p}\Delta T_{99,30\text{min}}$  is 0.136 °C (2E and 2F). Figure S3 shows temperature rise versus time for a scenario with constant perfusion and temperature dependent perfusion. In the case of temperature dependent perfusion, a steady state is achieved within 30 min. If we use temperature simulations with constant perfusion parameters, which is necessary with temperature VOPs, we will obtain a conservative estimate of temperature rise after a steady state is achieved.

### 3.4 | RF shimmed SAR and temperature analysis

The transmit phases and input powers that were used for the different RF shims are shown for every model in Figure 3.

A wide variability is observed in input phases for different models, but also for different shim settings within the same model. For the transmit amplitudes, variation between models and shims is smaller for the subject-specific RF shimming methods. The transmit phases that were used for the universal RF shim all remain within the range spanned by the transmit phases of the subject-specific RF shims, except for Channel 4, where a very wide variability is observed among transmit phases between models and between different RF shims. Surprisingly, the transmit powers of the universal RF shim differ strongly from the transmit powers of the subject-specific RF shims, which indicates that the shimming algorithm converged to another minimum.

For different RF shimming methods, average  $B_1^+$ , coefficient of variation of  $B_1^+$ , peak SAR and peak  $\Delta T$  values were calculated. The values are shown for each volunteer and for the whole dataset on average in Figure 4.

As expected, the max  $B_1^+$  shim leads to the highest average  $B_1^+$  in the heart (average over all volunteers 0.27, 0.23, 0.17 and 0.20  $\mu\text{T}$  for max, tradeoff, homogeneity and universal shims). The homogeneity shim leads to the lowest coefficient of variation of  $B_1^+$  in the heart (average

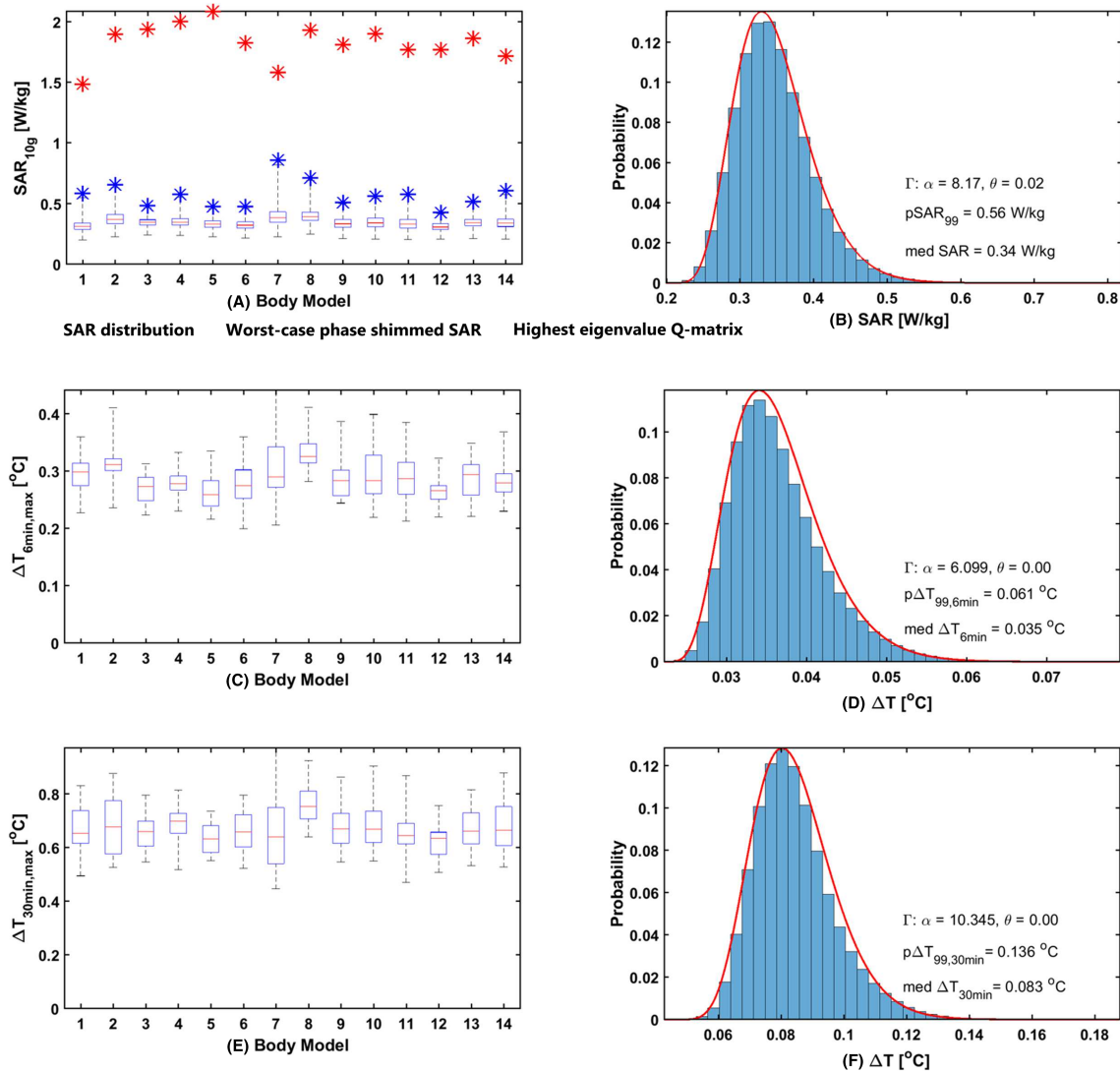


**FIGURE 2** Peak  $SAR_{10g}$  and  $\Delta T$  values for 100 000 random RF shims with a total average power of 1 W, specified for every model. The left-hand column of the graph shows the distribution of  $SAR_{10g}$  and  $\Delta T$  values for the individual models. A, B,  $SAR_{10g}$  values; C-F,  $\Delta T$  values; the heating interval is specified in the axis label. Temperature rise was calculated for different heating intervals. A gamma distribution was fitted to the histograms (indicated in red) to enable fitting of distribution parameters such as median values and 99.9% confidence intervals

27, 20, 16 and 23% for max, tradeoff, homogeneity and universal shims). There is no clear relationship between shimming method and peak SAR (average 0.33, 0.35, 0.34, 0.34 W/kg for max, tradeoff, homogeneity and universal shims) or temperature rise (average 0.035, 0.036, 0.034, 0.036 °C for max, tradeoff, homogeneity and universal shims). Supplementary Figure S4 shows the same results as Figure 4, but with BMI on the x-axis. There is a moderate negative correlation between BMI and average  $B_1^+$ , max SAR and max  $\Delta T$  (Pearson correlation coefficient  $R = -0.48$ ,  $-0.54$  and  $-0.48$  respectively) and a moderate positive correlation ( $R = 0.43$ ) between coefficient of variation and BMI. Figures 5, 6 and 7 show respectively the  $B_1^+$  fields, the  $SAR_{10g}$  distributions and the  $\Delta T$  distributions when applying subject-specific max  $B_1^+$  shims.

The highest average  $B_1^+$  in the heart is observed in Volunteer 7 (0.37  $\mu T$  for 1 W total input power). The highest SAR and peak  $\Delta T$  values are also observed in Volunteer 7 (0.45 W/kg and 0.046 °C for 1 W input power) in the left lower back muscle. The same distributions, but for the homogeneity shim, the tradeoff shim and the universal RF shim are added as supplementary material (S5, S6 and S7). Figure 8 shows histograms of the peak SAR and  $\Delta T$  values for subject-specific phase-amplitude shimming.

A gamma distribution was fitted to the histogram, resulting in a  $pSAR_{99}$  of 0.57 W/kg (median SAR 0.34 W/kg) and a  $p\Delta T_{99}$  of 0.057 °C (median  $\Delta T$  0.035 °C). The same results are shown for subject specific phase-only RF shimming (Figure S8, max SAR 0.68 W/kg, max  $\Delta T$  0.063 °C) and for RF shimming with the same universal shims as used for every model (Figure S9, max SAR 0.57 W/kg, max  $\Delta T$  0.057 °C). Since the histograms in Figures S8 and S9 do not correspond to normal or gamma distributions, these distributions were not fitted and we calculate the maximum SAR value in the database instead of the  $pSAR_{99}$  value.

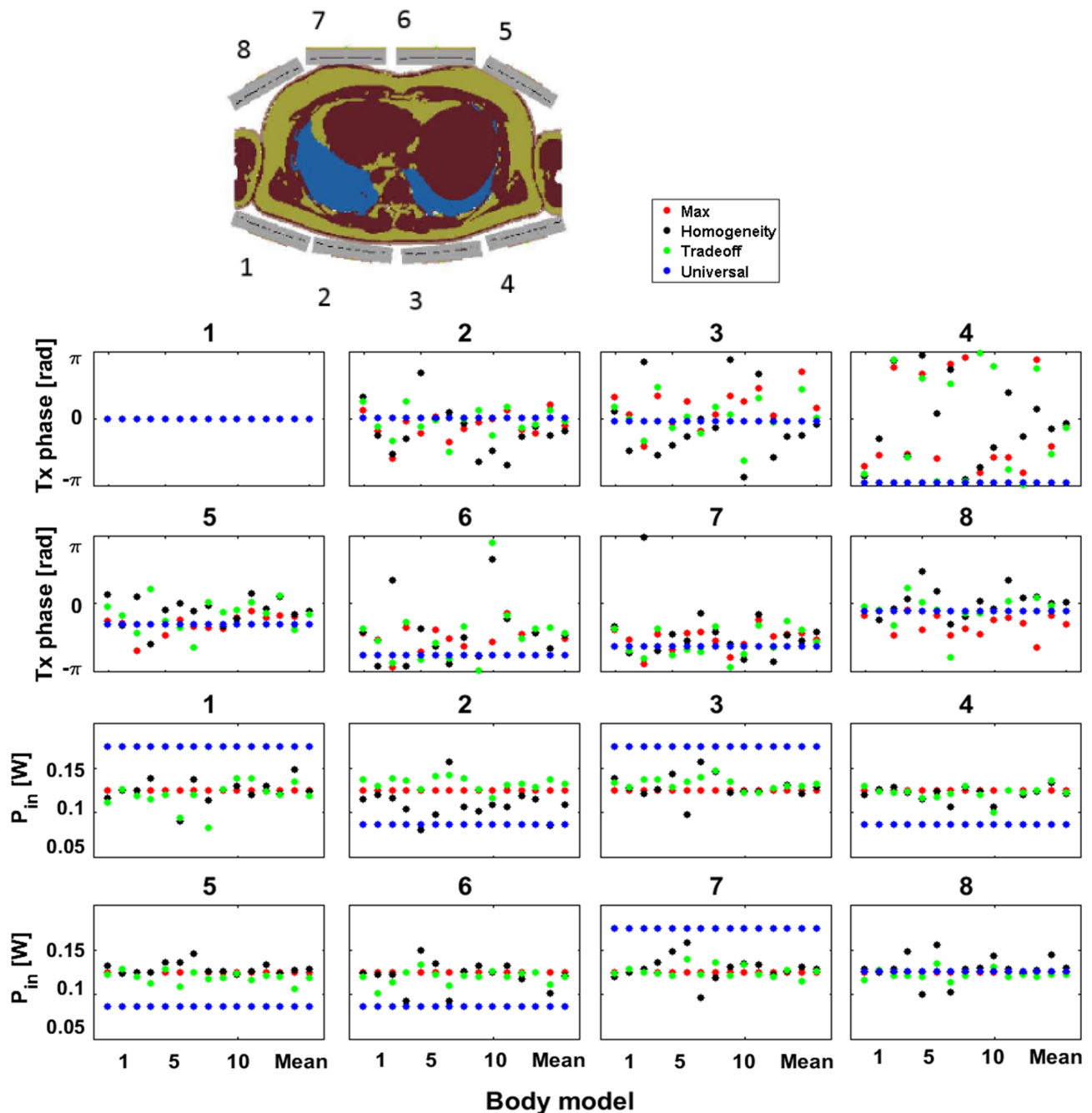
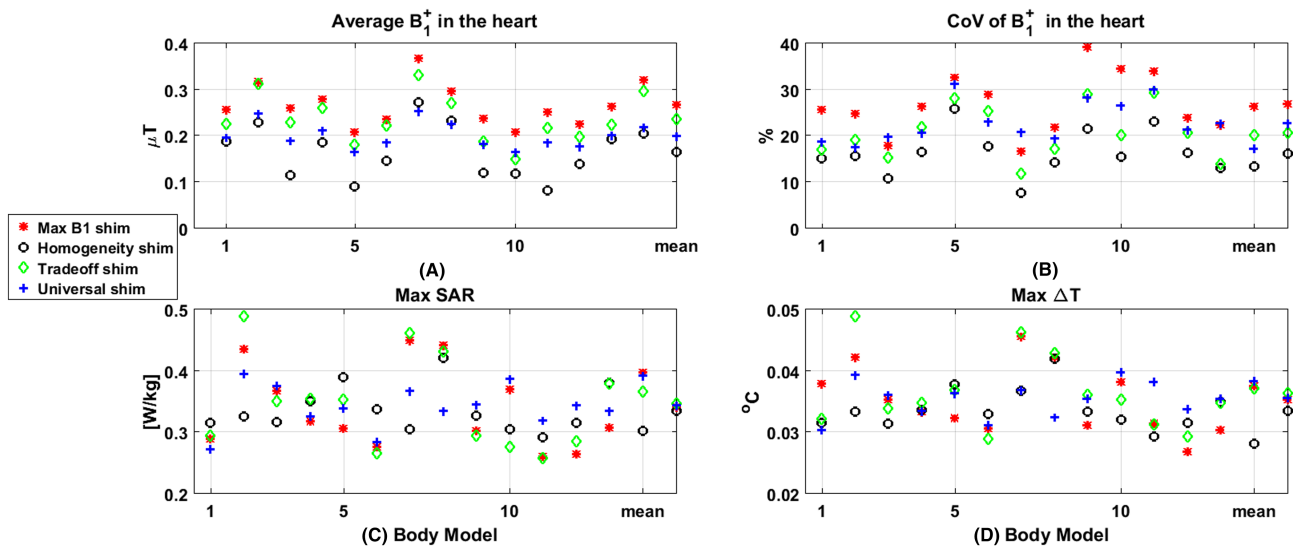


**FIGURE 3** Transmit phase (top two rows) and input power (bottom two rows) for every transmit channel and for all subjects for the different RF shimming methods. Channel numbers are indicated in Model 1

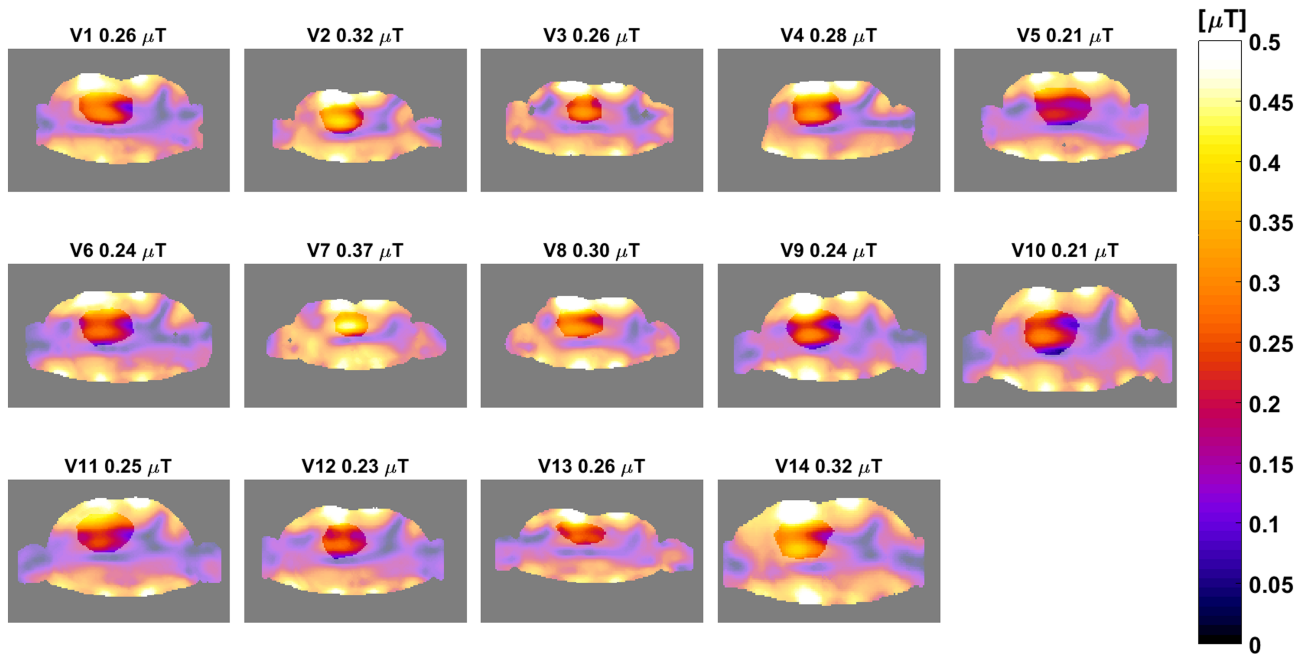
### 3.5 | Correlation between peak $SAR_{10g}$ and $\Delta T$

Figure 9 shows the correlation between peak  $SAR_{10g}$  and peak  $\Delta T$  (heating interval 6 min) values for the same RF shims. A strong correlation (Pearson correlation coefficient  $r = 0.77$ ) is observed between the 10 g-averaged SAR values and the  $\Delta T$  values. It can also be observed from Figure 9 that in many cases a simple linear model to predict peak temperature from peak SAR could potentially lead to severe underestimation of temperature.

Finally, we investigated the effect of dropping models from our database; the results of this analysis are shown in Figure S10. For the shims with random phases and uniform input power, the effect of dropping multiple models from the database on the SAR and temperature histogram is very small even when three or five models are used in the database. For the subject-specific RF shimming methods, the effect of dropping models from the database is more evident: when three models are used in the database, the shape of the SAR histogram changes.



**FIGURE 4** Mean  $B_1^+$  in the heart ROI, coefficient of variation (CoV) of  $B_1^+$ , peak SAR and peak  $\Delta T$  values for the different shim methods plotted for all volunteers and averaged over all volunteers



**FIGURE 5** Transverse slice (centered on the heart) of the  $B_1^+$  field for every subject, after application of RF shimming on the ROI in the heart. The ROI is indicated as non-transparent. A total input power of 1 W was applied. The average  $B_1^+$  in the ROI is indicated above the field distribution

## 4 | DISCUSSION

The inter-subject variation of  $B_1^+$ , SAR and temperature distributions was determined for cardiac imaging at 7 T using an eight-channel fractionated dipole array. The results of this work are specific for the eight-channel dipole array but give an indication of inter-subject variation for 7 T body imaging and cardiac imaging. When comparing the RF shimmed  $B_1^+$  distributions in all volunteers, the highest average  $B_1^+$ , SAR and temperature rises were found in Model 7, which also has the lowest BMI (17.9). This is in line with our finding of a weak negative correlation between these parameters and BMI. For random input phases, a  $pSAR_{99}$  of 0.56 W/kg was found for 1 W input power. In first level controlled mode, this implies that a total input power of 35.7 W (4.5 W/channel) can be allowed before a  $pSAR_{99}$  of 20 W/kg is achieved. For random perturbations on subject-specific amplitude and phase RF shims, a  $pSAR_{99}$  of 0.57 W/kg was found, which results in a total power limit of 35.0 W (4.4 W/channel).



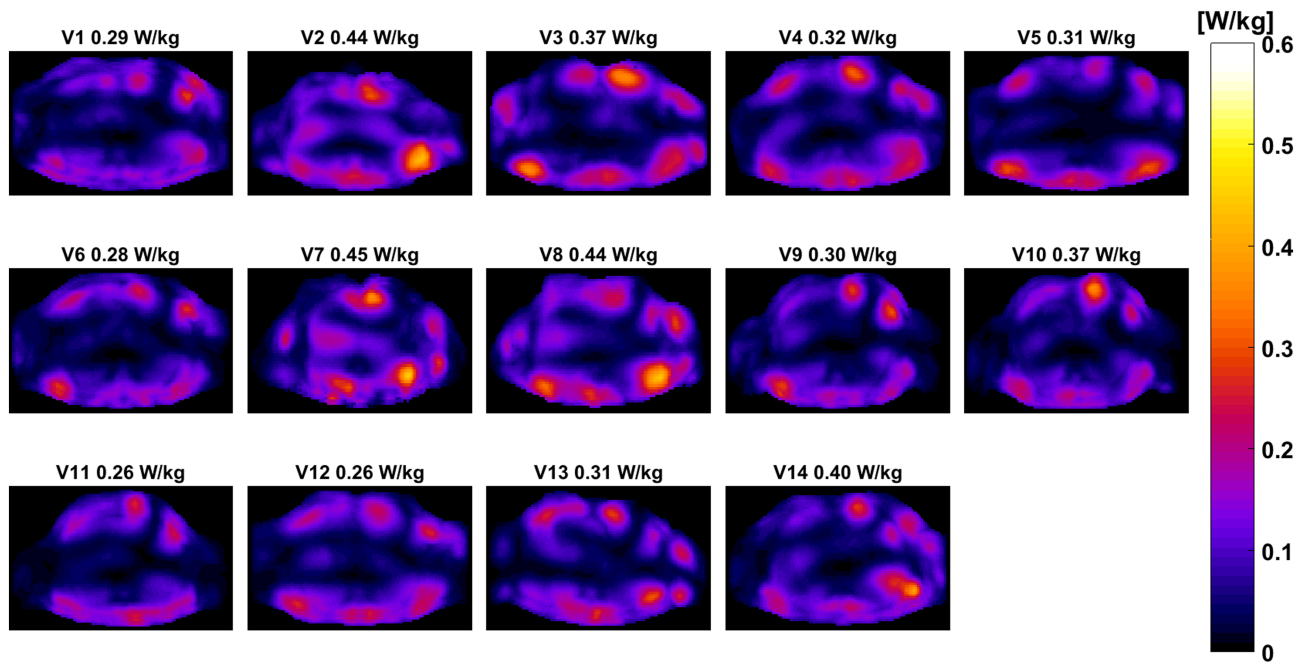


**FIGURE 6** Transverse maximum intensity projection of the SAR<sub>10g</sub> distribution and the peak SAR<sub>10g</sub> value for every subject after application of RF shimming (Max  $B_1^+$  shim) using 1 W total input power

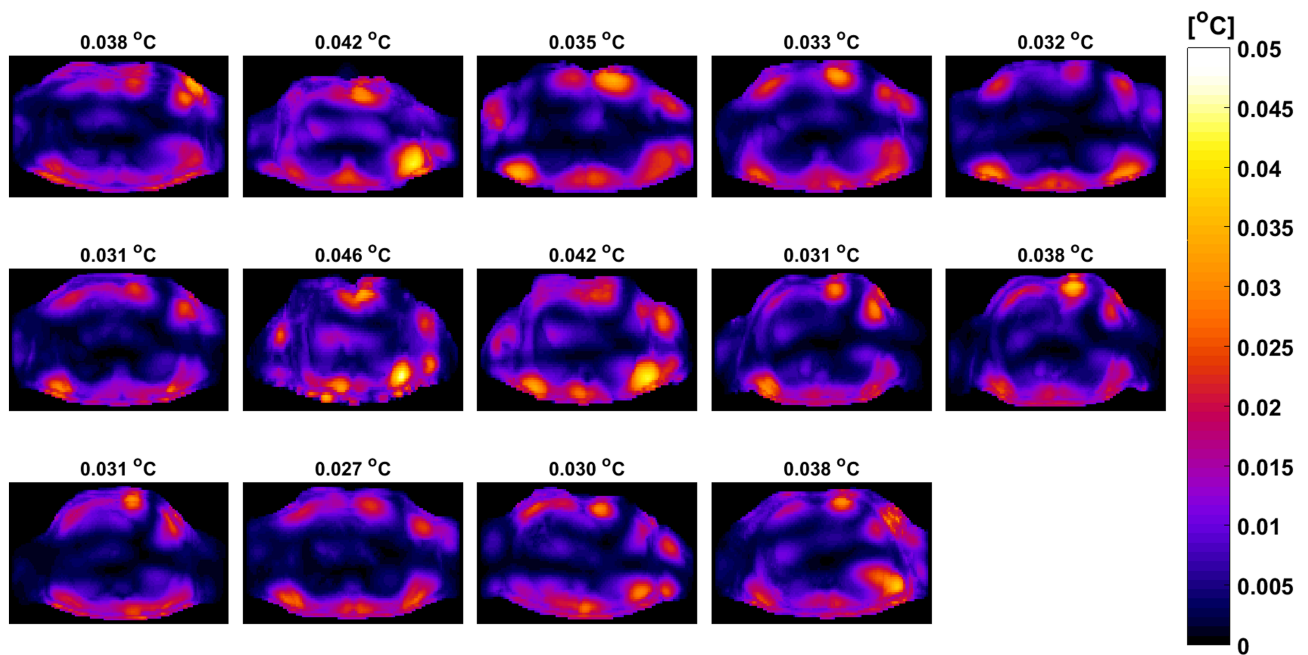


**FIGURE 7** Transverse maximum intensity projection of the peak  $\Delta T$  value for every subject after application of RF shimming (Max  $B_1^+$  shim) and a heating period of 6 min at a total input power of 1 W

When using a universal RF shim, a maximum SAR of 0.57 W/kg was found, resulting in a total power limit of 35.0 (4.4 W/channel). Finally, for subject-specific phase-only RF shimming, a maximum SAR of 0.68 W/kg was found, resulting in a total power limit of 29.4 W (3.7 W/channel).

When displaying the peak SAR values for all volunteers and random RF phase shims in a histogram, the result is a distribution of SAR values that corresponds to a gamma distribution in the case of phase-only shimming. We hypothesize that this is because the electric fields have a normal distribution, and the SAR is calculated from the electric field squared, resulting in a gamma distribution. The fitted gamma distribution results in a SAR value that is not exceeded for 99.9% of all random RF shim settings<sup>11</sup> ( $p\text{SAR}_{99}$ ). The significance of the  $p\text{SAR}_{99}$  value is that we know

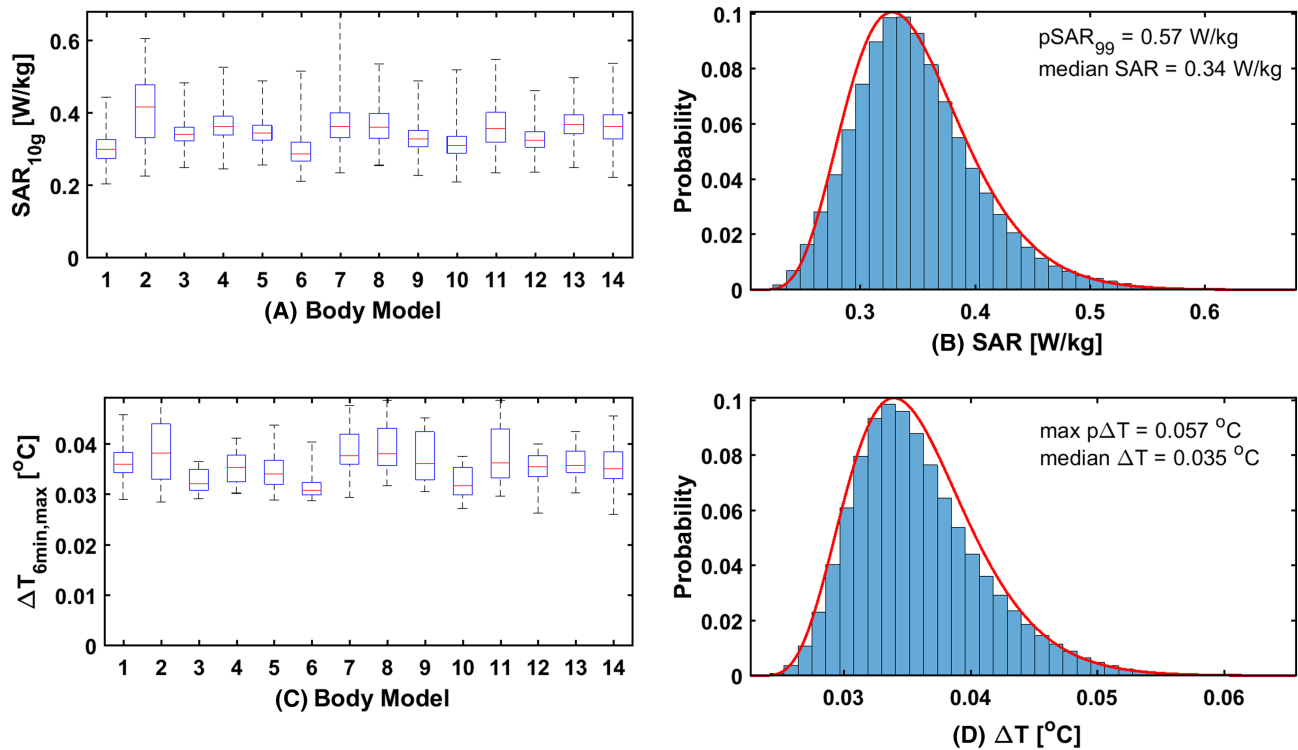
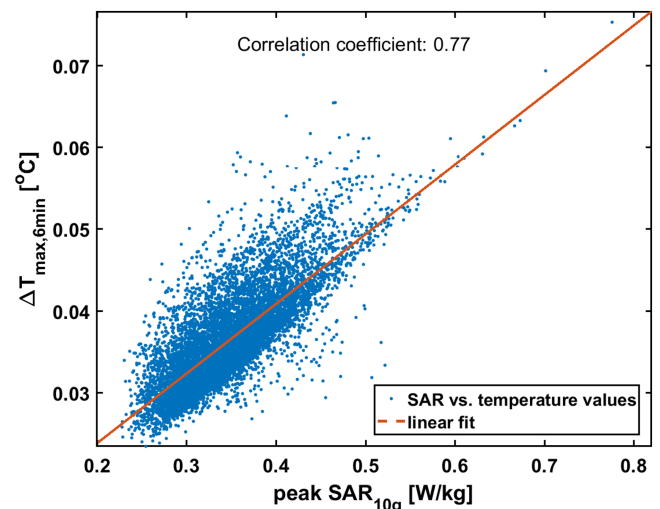


**FIGURE 8** SAR and temperature distributions for a scenario where subject-specific RF shimming is performed on the heart. In the left-hand column, bar plots indicate the SAR distribution per mode, while in the right-hand column a histogram of SAR and temperature values is shown for all models. The gamma distribution that was fitted to the histogram is indicated in red. For every volunteer, 100,000 shim vectors were calculated, which are random perturbations on the max, homogeneity or tradeoff shim, uniformly sampled from a range within  $\pm 10\%$  of the amplitudes and phases that were used for the initial shim

**FIGURE 9** Peak  $\Delta T$  values for a heating time of 6 min plotted versus peak 10 g-averaged local SAR values for the same RF shim drives



that the chance of exceeding the SAR limit is very low (0.1%); therefore, we have a realistic but not overly conservative upper bound to the peak SAR. If the small likelihood of extremely large SAR levels is to be taken into account, it is possible to calculate over all the models the peak SAR value in the database. For this calculation, we distinguish between a scenario with equal input power to all channels or a scenario with a fixed total input power, but input power may vary per channel. The maximum possible SAR level for the first scenario can be obtained by using the trigonometric method of Meliàdo et al.<sup>32</sup> Alternatively, the largest SAR value over 100 000 RF shims can be calculated; they coincide as indicated in Figure 2. The worst-case SAR when amplitudes are variable is equal to the maximum eigenvalue of the Q-matrices. Results in Figure 2 show that this value is extremely large because, for a surface array, it typically represents a situation where all input power is focused in one channel. This is demonstrated in Figure S10, where we calculated the SAR distribution for the eigenvector corresponding to the highest eigenvalue of the



Q-matrix. All power is deposited close to Antenna 7. With all energy focused on one antenna element, SAR levels under this element are expected to be large. Note that for both worst-case SAR scenarios there can still be a chance of exceeding the SAR limits because of inter-subject variation. The peak SAR value over all shims and models is in this sense less useful for our safety analysis as we do not know the accuracy of this value.

The probability of the worst-case peak SAR value actually taking place can be calculated by fitting a probability distribution to the simulated SAR values and then finding the probability of the worst-case peak SAR value. However, the actual worst-case peak SAR value will depend very much on the one worst-case model in the database, ie on the model database itself. Therefore, we choose to accept a certain pre-defined chance of underestimating SAR (0.1%) and we base our safety analysis on this accepted risk. This value should be the same for any sufficiently large database. Where we could not fit a Gaussian or a gamma distribution to the simulated SAR values, as was the case here for phase-only RF shimming or for the universal RF shim, the method did not work and it was required to use the peak SAR value over the whole database. The fact that it was not possible to fit a gamma distribution indicates that more models would be required to fully capture the SAR statistics when phase/amplitude shimming on the heart is performed.

Literature has shown that when calculating SAR limits based on one generic body model such as Duke or Ella<sup>10-12</sup> it is advised to take an additional safety factor into account to be robust for inter-subject variation and for variation in power measurements during the examination. For the random RF shims, a comparison of the median pSAR (0.34 W/kg) with the pSAR<sub>99</sub> (0.56 W/kg) value shows an average overestimation of 65%, which would translate into a safety factor of 1.65. If RF shimming is done, the worst-case pSAR value (0.57 W/kg) overestimates the median pSAR (0.34 W/kg) by 67%, leading to a safety factor of 1.67. In earlier studies, similar safety factors were reported for the prostate (1.7, Ipek et al,<sup>13</sup> 1.8 random, Meliàdò et al,<sup>11</sup> 1.4 RF shimmed, Meliàdò et al.<sup>11</sup>) and the head (1.5, Le Garrec et al,<sup>10</sup> 1.4, De Greef et al<sup>12</sup>). These results imply that the order of magnitude of inter-subject variation is comparable for different anatomies and coils, which provides more confidence when using general safety factors for coil arrays at 7 T. Since the pSAR<sub>99</sub> values resulting from this study include both inter-subject variability and variability in the RF shim phases and amplitudes, these additional safety factors were not included. When considering the inter-subject variation of temperature, we found overestimation factors comparable to those of SAR. For random RF shims we found an overestimation of 74% (median p $\Delta T$  0.035 °C, p $\Delta T$ <sub>99</sub> 0.061 °C) and with RF shimming we found an overestimation of 62% (median p $\Delta T$  0.035 °C, p $\Delta T$ <sub>99</sub> 0.057 °C).

As indicated by the results in Figure S10, the distributions of peak SAR values for random RF phases and equal input power show only small changes when models are dropped from the database. This provides confidence in pSAR<sub>99</sub> values for subjects that do not deviate strongly from the models in our database. When amplitude shimming is performed on the heart, the effect of dropping models from the database is somewhat larger: it can be observed that when three models are used in the database the shape of the SAR histogram changes strongly.

Pennes' bioheat equation, combined with a post-processing step to rapidly combine multi-channel temperature simulation results, was used to quickly calculate peak temperature rise values using 100 000 RF shims for each of our 14 custom-built models. A probabilistic analysis of peak  $\Delta T$  values was done for two scenarios (6 min and 30 min). The simulations in Figure S3 indicate that for simulation times up to approximately 10 min there is no difference between simulated temperature for a situation with or without temperature dependent perfusion parameters. Therefore, our temperature matrix implementation is in this limit consistent with the full Pennes bioheat model. However, for simulations of 30 min, there is a large difference between the two scenarios. Assuming that perfusion increases with temperature,<sup>37</sup> our 30 min results are overestimating the temperature rise. It appears that for longer averaging times and higher temperatures the temperature VOP approach cannot provide accurate predictions of temperature rise, since temperature dependent perfusion effects come into play. In addition, the VOP compression approach in general introduces overestimation for SAR and temperature calculations. In future work, alternative methods such as demonstrated by Pendse et al<sup>41</sup> can be used to make rapid calculations of SAR without overestimation.

For the 6 min heating interval and a total average input power of 1 W divided equally over all channels, a p $\Delta T$ <sub>99,6min</sub> value of 0.061 °C is found. When adhering to the local SAR limit of 20 W/kg in the trunk in first level controlled mode, an average power limit of 35.7 W would be allowed. This implies that when adhering to the local SAR limits the p $\Delta T$ <sub>99,30min</sub> value would be equal to 2.18 °C. In the case of subject-specific RF shimming, a p $\Delta T$ <sub>99,6min</sub> value of 0.057 °C is found for 1 W total input power. When adhering to the SAR-based average power limit of 35.0 W, the p $\Delta T$ <sub>99,6min</sub> value would be 2.00 °C. As defined by the IEC, local tissue temperature may not exceed 40 °C in the first level controlled mode. Assuming that the starting equilibrium temperature of the tissue in the VOP with maximum temperature rise is 37 °C, and according to Pennes' bioheat model and the thermal parameters found in the literature, a local temperature of 40 °C will not be achieved when adhering to the SAR limits for heating intervals of 6 min. For the 30 min heating interval, a p $\Delta T$ <sub>99,30min</sub> value of 0.136 °C is found for 1 W input power, which would result in a temperature rise of 4.9 °C when operating at the SAR limit (input power 35.7 W) In this case, the temperature limit of 40 °C could be exceeded. However, it has to be noted that the temperature VOP approach likely overestimates the temperature rise for the 30 min heating interval. The thermoregulatory response (perfusion increases with temperature rise) is not included in this model, which is expected to result in considerable overestimation of temperature rise when temperatures exceed 40 °C.<sup>37,38,42</sup> All simulations were done using perfusion values from the literature. However, cases in which subjects have a decreased perfusion response were not considered within the scope of this work. Furthermore, another that was not considered in this work was the duty cycle of the MRI sequence. For example, it is highly unlikely that during a 30 min MRI examination 100% SAR will be applied all the time. The examination is usually split into several sequences with different SAR levels and breaks in between. The scenario in which local tissue temperature exceeds the temperature limit during a 30 min or longer MRI scan therefore becomes more unlikely.

It is important to note that all temperature distributions shown here refer to temperature rise (which scales linearly with input power), and not absolute temperature (not linear with input power). Since the equilibrium temperature is generally lower close to the surface of a subject,

absolute temperature is likely overestimated by adding the temperature rise to a baseline temperature of 37 °C. Scenarios where the starting temperature is higher than 37 °C due to metabolic heat generation from exercise or fever were not considered.

## 5 | CONCLUSION

In this work we investigated the inter-subject variation of SAR and temperature rise for 7 T cardiac imaging with an eight-channel dipole array. Based on our study in 14 dielectric models, we found safe power limits for subject-specific RF shims which have good  $B_1^+$  coverage in the heart (total power limit 35.0 W) and for RF shims with random phase and uniformly distributed input power (total power limit 35.7 W). Our results indicate that inter-subject variation lies between 65% and 67% for peak SAR, and between 62% and 74% for peak temperature. When adhering to the SAR limits as specified by the IEC in first level controlled mode, the local tissue temperature limit of 40 °C in first level controlled mode is unlikely to be exceeded for a 6 min exposure time at the local SAR limit. To make statements about scan intervals of 30 min, the effect of temperature dependent perfusion parameters needs to be considered.

## ACKNOWLEDGEMENT

This research was funded by the Dutch Research Council (NWO), grant no. 15739.

## DATA AVAILABILITY STATEMENT

The data that support the findings of this study (segmented dielectric body models) are available on request from the corresponding author. The data are not publicly available due to privacy or ethical restrictions.

## ORCID

Bart R. Steensma  <https://orcid.org/0000-0002-4254-9937>

Ettore F. Meliàdò  <https://orcid.org/0000-0003-1240-3141>

Peter Luijten  <https://orcid.org/0000-0002-8040-8449>

Dennis W. J. Klomp  <https://orcid.org/0000-0002-5884-5386>

Cornelis A. T. van den Berg  <https://orcid.org/0000-0002-5565-6889>

Alexander J. E. Raaijmakers  <https://orcid.org/0000-0001-7111-330X>

## REFERENCES

- Oezerdem C, Winter L, Graessl A, et al. 16-channel bow tie antenna transceiver array for cardiac MR at 7.0 tesla. *Magn Reson Med*. 2016;75(6):2553-2565. <https://doi.org/10.1002/mrm.25840>
- Graessl A, Renz W, Hezel F, et al. Modular 32-channel transceiver coil array for cardiac MRI at 7.0T. *Magn Reson Med*. 2014;72(1):276-290. <https://doi.org/10.1002/mrm.24903>
- Steensma BR, Voogt IJ, Leiner T, et al. An 8-channel Tx/Rx dipole array combined with 16 Rx loops for high-resolution functional cardiac imaging at 7 T. *Magn Reson Mater Physics Biol Med*. 2017;31(1):7-18. <https://doi.org/10.1007/s10334-017-0665-5>
- Kramer CM, Barkhausen J, Flamm SD, Kim RJ, Nagel E. Standardized cardiovascular magnetic resonance (CMR) protocols 2013 update. *J Cardiovasc Magn Reson*. 2013;15(91). <https://doi.org/10.1186/1532-429X-15-91>
- Collins CM, Liu W, Wang J, et al. Temperature and SAR calculations for a human head within volume and surface coils at 64 and 300 MHz. *J Magn Reson Imaging*. 2004;19(5):650-656.
- Vaughan JT, Garwood M, Collins CM, et al. 7T vs. 4T: RF power, homogeneity, and signal-to-noise comparison in head images. *Magn Reson Med*. 2001;46(1):24-30. <https://doi.org/10.1002/mrm.1156>
- IEC. *Medical Electrical Equipment. Part 2-33: Particular Requirements for the Safety of Magnetic Resonance Equipment for Medical Diagnosis*. 2015. IEC 60601-2-33.
- Christ A, Kainz W, Hahn EG, et al. The Virtual Family—development of surface-based anatomical models of two adults and two children for dosimetric simulations. *Phys Med Biol*. 2010;55(2):N23-N38. <https://doi.org/10.1088/0031-9155/55/2/N01>
- Boulant N, Gras V, Amadon A, Luong M, Ferrand G, Vignaud A. Workflow proposal for defining SAR safety margins in parallel transmission. Paper presented at: Joint Annual Meeting ISMRM-ESMRMB; June 16-21, 2018; Paris, France. 0295.
- Le Garrec M, Gras V, Hang MF, Ferrand G, Luong M, Boulant N. Probabilistic analysis of the specific absorption rate intersubject variability safety factor in parallel transmission MRI. *Magn Reson Med*. 2017;78(3):1217-1223. <https://doi.org/10.1002/mrm.26468>
- Meliàdò EF, van den Berg CAT, Luijten PR, Raaijmakers AJE. Intersubject specific absorption rate variability analysis through construction of 23 realistic body models for prostate imaging at 7T. *Magn Reson Med*. 2018;81(3):2106-2119. <https://doi.org/10.1002/mrm.27518>
- De Greef M, Ipek O, Raaijmakers AJE, Crezee J, Van Den Berg CAT. Specific absorption rate intersubject variability in 7T parallel transmit MRI of the head. *Magn Reson Med*. 2013;69(5):1476-1485. <https://doi.org/10.1002/mrm.24378>
- Ipek Ö, Raaijmakers AJ, Legendijk JJ, Luijten PR, Van Den Berg CAT. Intersubject local SAR variation for 7T prostate MR imaging with an eight-channel single-side adapted dipole antenna array. *Magn Reson Med*. 2014;71(4):1559-1567. <https://doi.org/10.1002/mrm.24794>
- Raaijmakers AJE, Ipek O, Klomp DWJ, et al. Design of a radiative surface coil array element at 7 T: the single-side adapted dipole antenna. *Magn Reson Med*. 2011;66(5):1488-1497. <https://doi.org/10.1002/mrm.22886>
- Massire A, Cloos MA, Luong M, et al. Thermal simulations in the human head for high field MRI using parallel transmission. *J Magn Reson Imaging*. 2012;35(6):1312-1321. <https://doi.org/10.1002/jmri.23542>

16. Boulant N, Wu X, Adriany G, Schmitter S, Uğurbil K, Van De Moortele PF. Direct control of the temperature rise in parallel transmission by means of temperature virtual observation points: simulations at 10.5 tesla. *Magn Reson Med*. 2016;75(1):249-256. <https://doi.org/10.1002/mrm.25637>
17. Deniz CM, Carluccio G, Collins C. Parallel transmission RF pulse design with strict temperature constraints. *NMR Biomed*. 2017;30(5):e3694-e3694. <https://doi.org/10.1002/nbm.3694>
18. Destruel A, O'Brien K, Jin J, Liu F, Barth M, Crozier S. Adaptive SAR mass-averaging framework to improve predictions of local RF heating near a hip implant for parallel transmit at 7 T. *Magn Reson Med*. 2019;81(1):615-627. <https://doi.org/10.1002/mrm.27379>
19. Li X, Rispoli JV. Toward 7T breast MRI clinical study: safety assessment using simulation of heterogeneous breast models in RF exposure. *Magn Reson Med*. 2019;81(2):1307-1321. <https://doi.org/10.1002/mrm.27395>
20. Maspero M, Seevinck PR, Meijer GJ, Lagendijk JJW, Viergever MA, van den Berg CAT. SU-E-J-219: a Dixon based pseudo-CT generation method for MR-only radiotherapy treatment planning of the pelvis and head and neck. *Med Phys*. 2015;42(6):3316-3316. <https://doi.org/10.1118/1.4924305>
21. Gabriel S, Lau RW, Gabriel C. The dielectric properties of biological tissues: II. Measurements in the frequency range 10 Hz to 20 GHz. *Phys Med Biol*. 1996;41(11):2251-2269. <https://doi.org/10.1088/0031-9155/41/11/002>
22. McIntosh RL, Anderson V. A comprehensive tissue properties database provided for the thermal assessment of a human at rest. *Biophys Rev Lett*. 2010;05(03):129-151. <https://doi.org/10.1142/S1793048010001184>
23. Homann H, Börner P, Eggers H, Nehrke K, Dössel O, Graesslin I. Toward individualized SAR models and in vivo validation. *Magn Reson Med*. 2011;66(6):1767-1776. <https://doi.org/10.1002/mrm.22948>
24. Doran E, Bawden S, Bowtell W, Gowland PA, Glover P. Simplified subject-based models for efficient electromagnetic simulations and evaluation of local SAR for 7 T abdominal MRI. Paper presented at: ISMRM 27th Annual Meeting & Exhibition; May 11-16, 2019; Montreal, Canada. 4156.
25. Carluccio G, Akgun C, Vaughan JT, Collins CM. Temperature-based MRI safety assessment with a simplified body model. Paper presented at: ISMRM 27th Annual Meeting & Exhibition; May 11-16, 2019; Montreal, Canada. 4161.
26. Raaijmakers AJE, Italiaander M, Voogt IJ, et al. The fractionated dipole antenna: a new antenna for body imaging at 7 Tesla. *Magn Reson Med*. 2016;75(3):1366-1374. <https://doi.org/10.1002/mrm.25596>
27. Carluccio G, Erricolo D, Oh S, Collins CM. An approach to rapid calculation of temperature change in tissue using spatial filters to approximate effects of thermal conduction. *IEEE Trans Biomed Eng*. 2013;60(6):1735-1741. <https://doi.org/10.1109/TBME.2013.2241764>
28. Oh S, Carluccio G, Collins CM. Method and tool for improved rapid N-gram average SAR determination. Paper presented at: ISMRM 19th Annual Meeting & Exhibition; May 7-13, 2011; Montreal, Canada. 3868.
29. Eichfelder G, Gebhardt M. Local specific absorption rate control for parallel transmission by virtual observation points. *Magn Reson Med*. 2011;66(5):1468-1476. <https://doi.org/10.1002/mrm.22927>
30. Lee J, Gebhardt M, Wald LL, Adalsteinsson E. Local SAR in parallel transmission pulse design. *Magn Reson Med*. 2012;67(6):1566-1578. <https://doi.org/10.1002/mrm.23140>
31. Kuehne A, Waiczies H, Niendorf T. Massively accelerated VOP compression for population-scale RF safety models. Paper presented at: ISMRM 25th Annual Meeting & Exhibition; April 22-27, 2016; Singapore. 0478.
32. Melià EF, Sbrizzi A, van den Berg CAT, Luijten PR, Raaijmakers AJE. Real-time assessment of potential peak local specific absorption rate value without phase monitoring: Trigonometric maximization method for worst-case local specific absorption rate determination. *Magn Reson Med*. 2020;85:3433-3420. <https://doi.org/10.1002/mrm.28635>
33. Pennes HH. Analysis of tissue and arterial blood temperatures in the resting human forearm. *J Appl Physiol*. 1948/1998;85(1):5-34. <https://doi.org/10.1152/jappl.1998.85.1.5>
34. Das SK, Clegg ST, Samulski TV. Computational techniques for fast hyperthermia temperature optimization. *Med Phys*. 1999;26(2):319-328. <https://doi.org/10.1118/1.598519>
35. Guerin B. Matlab based temperature solver. [https://ptx.martinos.org/index.php/Matlab\\_based\\_temperature\\_solver](https://ptx.martinos.org/index.php/Matlab_based_temperature_solver). 2016.
36. Guérin B, Villena JF, Polimeridis AG, et al. Computation of ultimate SAR amplification factors for radiofrequency hyperthermia in non-uniform body models: impact of frequency and tumour location. *Int J Hyperthermia*. 2017;34(1):87-100.
37. Laakso I, Hirata A. Dominant factors affecting temperature rise in simulations of human thermoregulation during RF exposure. *Phys Med Biol*. 2011;56(23):7449-7471. <https://doi.org/10.1088/0031-9155/56/23/008>
38. Murbach M, Neufeld E, Cabot E, et al. Virtual population-based assessment of the impact of 3 Tesla radiofrequency shimming and thermoregulation on safety and B<sub>1+</sub> uniformity. *Magn Reson Med*. 2016;76(3):986-997. <https://doi.org/10.1002/mrm.25986>
39. Gras V, Vignaud A, Amadon A, Le Bihan D, Boulant N. Universal pulses: a new concept for calibration-free parallel transmission. *Magn Reson Med*. 2017;77(2):635-643. <https://doi.org/10.1002/mrm.26148>
40. Melià EF, Raaijmakers AJE, Luijten PR, van den Berg CAT. Fast method to get an upper bound of the maximum SAR<sub>10g</sub> for body coil arrays. Paper presented at: Ninth Scientific Meeting ISMRM Benelux Chapter; 2017; Tilburg, The Netherlands. p-070.
41. Pendse M, Stara R, Mehdi Khalighi M, Rutt B. IMPULSE: a scalable algorithm for design of minimum specific absorption rate parallel transmit RF pulses. *Magn Reson Med*. 2019;81(4):2808-2822. <https://doi.org/10.1002/mrm.27589>
42. Simonis FFJ, Petersen ET, Bartels LW, Lagendijk JJW, Van Den Berg CAT. Compensating for magnetic field inhomogeneity in multigradient-echo-based MR thermometry. *Magn Reson Med*. 2015;73(3):1184-1189. <https://doi.org/10.1002/mrm.25207>

## SUPPORTING INFORMATION

Additional supporting information may be found online in the Supporting Information section at the end of this article.

**How to cite this article:** Steensma BR, Melià EF, Luijten P, Klomp DWJ, van den Berg CAT, Raaijmakers AJE. SAR and temperature distributions in a database of realistic human models for 7 T cardiac imaging. *NMR in Biomedicine*. 2021;34:e4525. <https://doi.org/10.1002/nbm.4525>